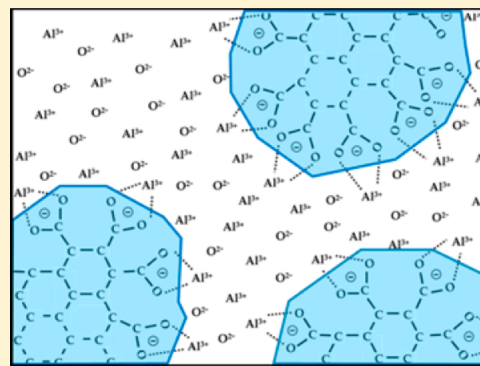


Pyrolysis of Alucone Molecular Layer Deposition Films Studied Using In Situ Transmission Fourier Transform Infrared Spectroscopy

Jaime W. DuMont[†] and Steven M. George^{*,†,‡}[†]Department of Chemistry and Biochemistry and [‡]Department of Mechanical Engineering, University of Colorado at Boulder, 215 UCB, Boulder, Colorado 80309, United States

ABSTRACT: The pyrolysis of alucone molecular layer deposition (MLD) films was studied in vacuum using in situ transmission Fourier transform infrared spectroscopy. The initial alucone MLD films were grown using trimethylaluminum (TMA) and either ethylene glycol (EG) (HO-(CH₂)₂-OH) or hydroquinone (HQ) (HO-C₆H₄-OH) at 150 °C. The alucone MLD films were then pyrolyzed in vacuum at temperatures ranging from 400 to 750 °C. The absorbance features for the C-H, C-C, and C-O stretching vibrations were observed to be lost at pyrolysis temperatures from 350 to 500 °C. For the alucone films grown using TMA and EG, the loss of these absorbance features was coupled to an increase in carboxylate (R-COO⁻) absorbance features. The carboxylate absorbance features reached their peak at a pyrolysis temperature of 450 °C and then decreased slowly with higher pyrolysis temperatures. The carboxylate absorbance features are consistent with an Al₂O₃/carbon composite material with Al³⁺/COO⁻ species at the interface. In addition, the presence of carbon in the Al₂O₃/carbon composite led to an increase in the background infrared absorbance for the pyrolyzed alucone films grown using HQ containing six carbons. This background infrared absorbance is linked to electrical conductance in a network of carbon domains in the pyrolyzed alucone films, as described by Drude-Zener theory. In contrast, the alucone films grown using EG containing two carbons did not display an increase in the background infrared absorbance. This absence of background infrared absorbance is consistent with less carbon in the Al₂O₃/carbon composite grown using EG. The pyrolysis of the alucone films on ZrO₂ particles led to very conformal Al₂O₃/carbon composite films, as observed by transmission electron microscopy images.



I. INTRODUCTION

Atomic layer deposition (ALD) and molecular layer deposition (MLD) are ideal techniques to deposit ultrathin inorganic and organic films.^{1–4} Both ALD and MLD are based on sequential, self-limiting surface reactions that allow conformal film growth on high aspect ratio structures with precise thickness control. The precursors for ALD and MLD can be combined to grow hybrid organic–inorganic metal alkoxide polymers known as “metalcones”.^{5,6} These hybrid MLD films can possess interesting mechanical and electrical properties.^{7,8} ALD and MLD can also be combined to form ALD/MLD alloys and nanolaminates that can be fine-tuned by varying the composition of the alloy.^{6,9,10}

Metalcone MLD films can also serve as a precursor to a new set of ceramic materials. Hybrid organic–inorganic MLD films can be annealed in air to burn out the carbon and yield porous metal oxide films.^{11–14} These porous metal oxide films have been shown to contain micropores and mesopores.¹¹ Hybrid organic–inorganic MLD films can also be pyrolyzed under vacuum or inert atmosphere to yield electrically conducting metal oxide/carbon composite films.¹⁵ This strategy is similar to the fabrication of ceramics from polymers in polymer-derived ceramic processing.¹⁶ These electrically conducting metal oxide/carbon composite films can display exceptionally low resistivity of ~0.2 Ω cm.¹⁵ Pure organic MLD films can also

be pyrolyzed under inert gas conditions to obtain carbon nanofilms.¹⁷

In the field of polymer-derived ceramics, the metal or metalloid is almost always limited to silicon.¹⁸ The conformality and distribution of the relative components of the film are also limited by the wet chemistry techniques used to prepare the polymer-derived ceramics.¹⁸ In contrast, MLD-derived ceramic films can be formed from a wide array of elements comprising metalcone MLD films such as Al,¹⁹ Zn,^{20,21} Zr,²² Hf,²³ and Ti.²⁴ Another important advantage of the pyrolysis of MLD films is that the initial MLD films can be formed conformally on initial substrates. After pyrolysis, the MLD-derived ceramic films maintain conformality with the substrate.¹⁹

Alucone is an aluminum alkoxide metalcone film grown using trimethylaluminum (TMA) and organic alcohols as the reactants. The first alucone films were grown using the sequential, self-limiting reactions of TMA and ethylene glycol (EG).¹⁹ Other alucone films have subsequently been grown using TMA with other alcohols such as glycerol.²⁵ Alucone

Special Issue: Steven J. Sibener Festschrift

Received: December 3, 2014

Revised: February 12, 2015

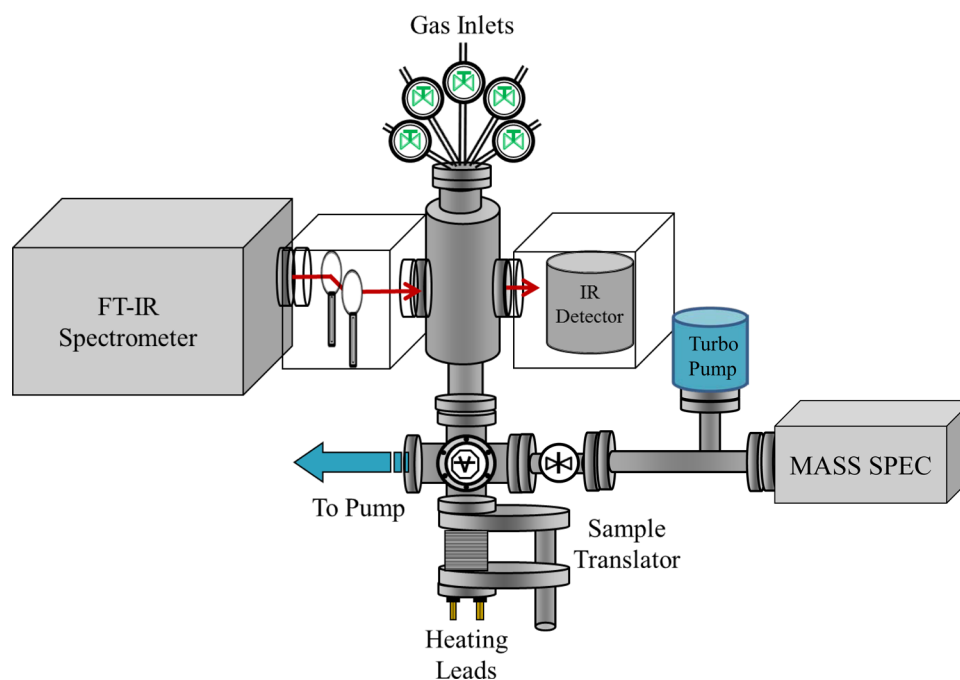


Figure 1. Schematic of MLD reactor designed to perform in situ transmission FTIR spectroscopy studies.

films have shown promise in a variety of applications. Alucone films have been employed for more flexible gas-diffusion barriers.^{26–28} Alucone films have also served as coatings to enhance gas-separation membranes²⁹ and as sacrificial layers to define air gaps.³⁰ In addition, alucone films have been used to protect Si anodes in Li ion batteries³¹ or stabilize sulfur cathodes in Li–S batteries.³²

In situ transmission Fourier transform infrared (FTIR) spectroscopy was used to study the pyrolysis of alucone MLD films. These alucone films were grown using the sequential deposition of TMA and either EG or hydroquinone (HQ). These alucone films were grown on ZrO₂ nanoparticles at 150 °C. The pyrolysis was then conducted in vacuum at pyrolysis temperatures of 400–750 °C. FTIR spectroscopy was used to study the vibrational absorption spectra of the alucone films versus pyrolysis temperature. These vibrational spectroscopy studies reveal the changes that occur within the alucone films during pyrolysis. These investigations also illustrate how pyrolyzed alucone films can produce an electrically conducting Al₂O₃/carbon composite film.

II. EXPERIMENTAL SECTION

A. Reactor Design. These studies were conducted in a viscous flow reactor equipped with an in situ FTIR spectrometer.^{21,33} A schematic of the reactor is shown in Figure 1. The reaction chamber consisted of a stainless-steel tube encased in an insulating ceramic shell. The reactor was maintained at 160 °C for all experiments using a 2604 Eurotherm PID temperature controller. The sample holder could be independently heated by flowing electrical current through the tungsten grid used to hold the sample.

Ultra-high-purity argon carrier gas was flowed through the reactor during deposition. The argon carrier gas passed continuously through the flow tube. The carrier gas flow was monitored by a capacitance monometer that could measure pressures down to 1×10^{-3} Torr. Reactant channels metered with pneumatic leak valves were used to facilitate rapid

switching between precursors. A Leybold TRIVAC D8B dual-stage rotary vane mechanical pump removed the argon, extra reactant, and reaction byproducts from the reactor.

The infrared beam was aligned to pass through the reaction chamber and the sample. The infrared windows were a pair of 0.5 in thick KBr windows supplied by International Crystal Laboratories. The windows were isolated from the vacuum chamber using gate valves to prevent the deposition of species that can interfere with the FTIR spectra. The sample stage was designed to translate the sample into and out of the IR beam.

The FTIR spectrometer employed in these studies was a Nicolet 6700 FTIR. The infrared signals were monitored using a high-sensitivity liquid-nitrogen-cooled mercury cadmium telluride (MCT-B) detector. The spectrometer, mirror, and detector setup were purged with dry, CO₂-free air. A total of 100 scans at 4 cm⁻¹ resolution from 400 to 4000 cm⁻¹ were recorded for each collected spectrum.

The reactor was equipped with an SRS RGA 200 amu quadrupole mass spectrometer. The mass spectrometer was differentially pumped with a 70 L/s turbomolecular pump. The mass spectrometer could be isolated from the reactor with a gate valve during film deposition. The turbomolecular pump could also lower the pressure in the reaction chamber during pyrolysis.

B. Sample Preparation/Sample Holder Design. The transmission FTIR measurements were performed on high-surface-area ZrO₂ nanoparticles (U.S. Research Nanomaterials) with an average diameter of 20 nm. The high surface area of these particles improved the signal-to-noise ratio compared with a flat sample.³⁴ Sample preparation involved pressing the ZrO₂ nanoparticles into a tungsten grid support.^{34,35} The tungsten grids were 2 × 3 cm². Each grid was 50 μm thick with 100 grid lines per inch. The tungsten grid sample supports were supplied by Tech-Etch.

The tungsten grid was first covered with an excess of ZrO₂ nanoparticles and placed into a stainless-steel die. The particles were then manually forced into the tungsten grid, and excess

nanoparticles were removed with a razor blade. This process resulted in a dense matrix of ~ 25 mg of ZrO_2 nanoparticles per tungsten grid. The corresponding surface area was ~ 0.8 m². To ensure good Ohmic contact, the edges of the tungsten grid were sandwiched on both sides between two strips of tantalum foil. The tantalum foil was then clamped between two stainless-steel bars that held the tungsten grid securely on the sample holder. The tantalum foil was obtained from Alfa Aesar.

The tungsten grid was resistively heated using a Hewlett-Packard 6268B power supply (20 V, 20A). The voltage output of the power supply was controlled by a Love Controls 16b PID temperature controller. A type-K thermocouple was attached to the bottom of the tungsten grid with Ceramabond 571 epoxy. The epoxy both attached and electrically isolated the thermocouple during sample heating.

A cleaning procedure of the ZrO_2 nanoparticles/grid support was used to produce consistent starting surfaces. Prior to alucone MLD, the temperature of the sample support was increased to 700 °C for ~ 2 min to degas and clean adventitious carbon from the ZrO_2 nanoparticles. Because this procedure also depleted hydroxyl groups from the ZrO_2 surface, a ~ 2 s H_2O dose was used to rehydroxylate the surface. This procedure consistently removed any carbon-related vibrational modes and resulted in a clean ZrO_2 starting surface with absorbances attributed only to the O–H hydroxyl stretching vibrations and bulk zirconia modes.

C. ALD and MLD Experimental Parameters. The alucone films were grown at 150 °C using TMA and either EG or HQ. The alucone films grown using TMA and EG are designated AIEG. The alucone films grown using TMA and HQ are designated AIHQ. The alucone MLD films were grown on Al_2O_3 ALD coatings on the ZrO_2 nanoparticles to ensure a reproducible starting surface. These Al_2O_3 ALD coatings were deposited using 10 Al_2O_3 ALD layers. The Al_2O_3 ALD was grown at 150 °C using TMA and H_2O as the reactants. The TMA and H_2O reactants were held at room temperature. The EG and HQ precursors were held at 85 and 145 °C, respectively. All reactants were obtained from Sigma-Aldrich.

The Al_2O_3 films were deposited using a 1.0 s TMA dose and a 1.0 s H_2O dose. These dose times produced ~ 350 and ~ 500 mTorr pressure transients above the base pressure, respectively. A 120 s purge time was used between each reactant exposure. The AIEG alucone films were deposited using a 1.0 s TMA dose and a 2.5 s EG dose. These dose times produced ~ 350 and ~ 40 mTorr pressure transients above the base pressure, respectively. A 200 s purge time was utilized between each reactant exposure. The AIHQ alucone films were deposited using a 1.0 s TMA dose and a 2.5 s HQ dose. These dose times produced ~ 300 and ~ 22 mTorr pressure transients above the base pressure, respectively. A 240 s purge time was used between each reactant exposure.

D. Pyrolysis Experimental Parameters. After the MLD films were deposited, the reactor chamber was isolated from the main mechanical pump and reduced to lower pressure of $\sim 1 \times 10^{-8}$ Torr using the turbomolecular pump. The tungsten grid support was then resistively heated from 150 to 750 °C at 50 °C intervals. Changes in the alucone film were monitored using in situ FTIR spectroscopy. For each temperature, the sample was quickly ramped to the desired temperature in ~ 5 s and held at temperature for ~ 15 s. To reduce thermal noise, the FTIR spectrum was obtained when the sample had cooled down to 150 °C. The FTIR spectra were referenced to the initial ZrO_2 powder coated with 10 cycles of Al_2O_3 ALD.

II. RESULTS AND DISCUSSION

In situ FTIR spectra of AIEG and AIHQ alucone films grown using 300 cycles of TMA and EG or TMA and HQ at 150 °C are shown Figure 2a,b, respectively. These FTIR spectra are

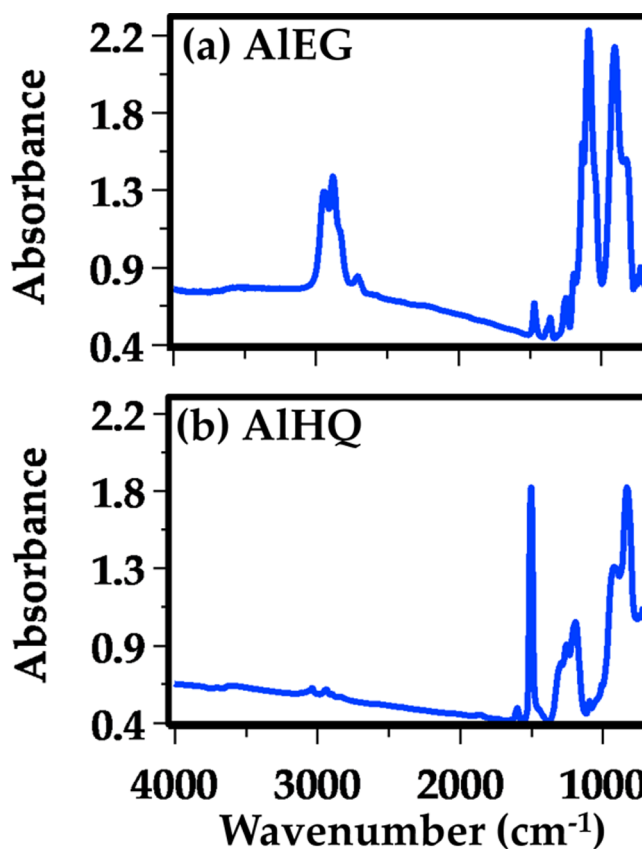


Figure 2. FTIR difference spectra of (a) AIEG alucone films grown using 300 cycles of TMA and EG at 150 °C and (b) AIHQ alucone films grown using 300 cycles of TMA and HQ at 150 °C. These difference spectra are referenced to the initial ZrO_2 powder coated with 10 cycles of Al_2O_3 ALD.

difference spectra referenced to the initial ZrO_2 powder with Al_2O_3 coating grown using 10 Al_2O_3 ALD cycles. The most prominent absorbances for the AIEG alucone film include the following: C–H stretching vibrations between 2700 and 2900 cm^{-1} ; C–C stretching vibrations at 1135 cm^{-1} ; C–O stretching vibrations at 1095 cm^{-1} ; and Al–O stretching vibrations at 910 cm^{-1} . These vibrational features are consistent with the previously reported peak assignments.¹⁹

For the AIHQ alucone film, a large distinctive absorbance feature is also observed at ~ 1500 cm^{-1} corresponding to the C=C vibrational stretching of the phenylene ring. The absorbance monitored at 1255–1290 cm^{-1} corresponds to the C–O stretching vibration. The absorbance observed between 830 and 900 cm^{-1} is attributed to the Al–O stretching vibrations in the alucone films.

Small absorbances are also observed between 3030–3065 cm^{-1} that correspond to the C–H stretching vibrations of the phenylene ring. Weak peaks corresponding to $-\text{CH}_3$ asymmetric and symmetric stretching vibrations between 2890–2940 cm^{-1} indicate that a small amount of unreacted $-\text{CH}_3$ groups are present in the film. Peak positions and assignments for the majority of the observed absorbances in the

AlHQ alucone film are given in Table 1.^{36–39} Some of the vibrational transitions are expressed using Wilson notation based on benzene modes.⁴⁰

Table 1. Infrared Peak Assignments for the AlHQ Alucone Film Displayed in Figure 2b

peak position (cm ⁻¹)	assignment
~3600	OH stretch
3065	20a ring C–H stretch
3030	20b ring C–H stretch
2940	CH ₃ asym stretch
2890	CH ₃ sym stretch
1600	8b ring C–C stretch
1500	19a ring C–C stretch
1290	C–O stretch, O–H bend
1255	C–O stretch
1212	Al–CH ₃ sym deform
1190	ring C–H bend
1095	18b ring C–H bend, O–H bend
1010	18a ring C–H bend
~900–830	Al–O stretch

In situ FTIR analysis also provided a means to monitor changes in the alucone films during pyrolysis. The pyrolysis of carbonaceous materials is very complex.⁴¹ Before presenting the results for the pyrolysis of AIEG and AlHQ, a brief general overview of the carbonization process is given below based on studies on a variety of organic polymers.

The carbonization of organic polymers can be divided into different chemical changes that occur at various temperatures during pyrolysis.^{41–44} Mass loss and FTIR studies indicate that chemical transformation in polymers and other carbonaceous materials begins to occur at ≥ 200 °C with the loss of H₂, CO, CO₂, and other small hydrocarbons such as CH₄ and C₂H₆.^{43,45,46} The release of these volatile products results from C–H and C–C bond cleavage to form reactive free radicals.⁴¹ These reactive free radicals then form polycyclic aromatic structures.^{41,47}

Most of the mass loss during carbonization occurs at ≤ 500 °C.^{42–44} At >500 °C, the polycyclic aromatic structures undergo progressive condensation with the release of additional H₂.⁴¹ The carbon becomes progressively more organized into hexagonal sp² planes with pyrolysis temperatures up to 800 °C. The Raman spectra of pyrolyzed organic polymers are also consistent with partially graphitized carbon.^{48,49} In addition, the pyrolyzed material can become electrically conducting.^{50–53} This electrical conductivity may depend on the number, size, and distribution of the sp² carbon domains.^{54,55}

A. Pyrolysis of AIEG Alucone Films Grown Using TMA and EG. Figure 3 shows the infrared absorbance of the AIEG alucone film prepared using 300 cycles of TMA and EG at 150 °C after various pyrolysis temperatures. For pyrolysis temperatures up to 350 °C, little change was observed in the infrared absorbance. The infrared absorbance of C–H, C–C, and C–O stretching vibrations then is rapidly reduced at ≥ 400 °C. This absorbance reduction is consistent with C–H, C–C, and C–O bond breakage within the alucone film.

An expansion of the infrared absorbance from 2600 to 3200 cm⁻¹ is shown in Figure 4a. This portion of the spectrum displays the infrared absorbance attributed to the CH₂ stretching vibrations within the film. The absorbance from the C–H stretching vibrations decreases as the C–H bonds

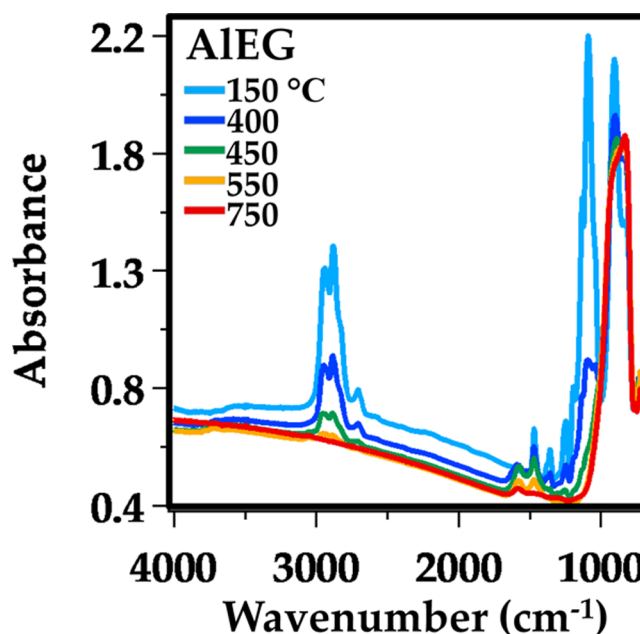


Figure 3. FTIR spectra of AIEG alucone film grown using 300 cycles that was pyrolyzed at progressively higher temperatures up to 750 °C. These difference spectra are referenced to the initial ZrO₂ powder coated with 10 cycles of Al₂O₃ ALD.

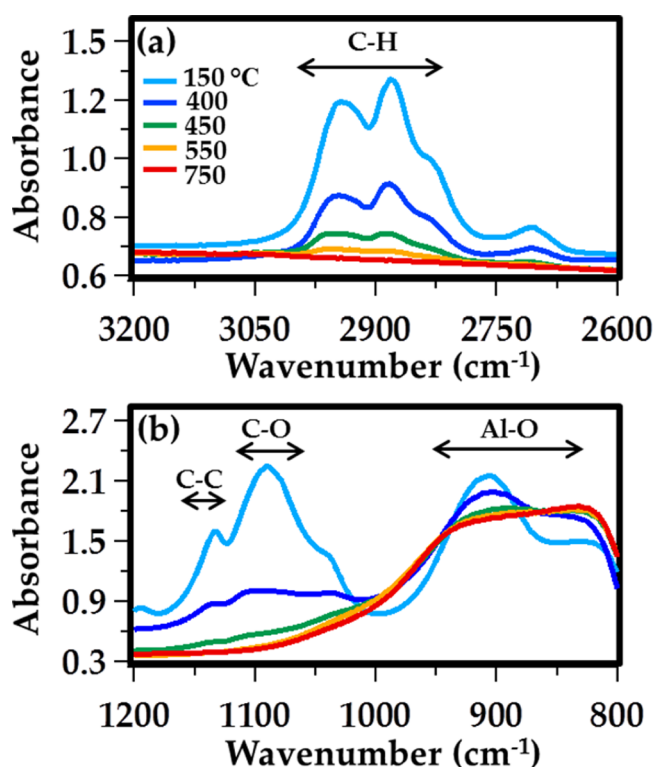


Figure 4. Expansion of FTIR spectra displayed in Figure 3 showing the effect of pyrolysis temperature on: (a) C–H stretching vibration region between 2600 and 3200 cm⁻¹ and (b) C–C, C–O, and Al–O stretching vibration regions between 800 and 1200 cm⁻¹.

within the films break at ~ 400 °C. All absorbances related to hydrogen within the alucone film were lost by 550 °C. The mass spectrometer monitored that this decrease in absorbance was accompanied by the release of a variety of gases such as H₂, H₂O, CO, CO₂, and light alkane gases. Some of these gases

could have resulted from outgassing produced by sample heating.

Figure 4b shows an expansion of the infrared absorbance from 800 to 1200 cm^{-1} . This portion of the spectrum includes absorbances related to the C–C and C–O stretching vibrations within the film. The C–C and C–O absorbance features at 1135 and 1095 cm^{-1} , respectively, follow a similar decreasing trend with temperature as the C–H features shown in Figure 4a.

The vibrational features shown in Figure 4b also include the absorbance related to the Al–O stretching vibrations in the film. These features shift toward lower wavenumbers with increasing pyrolysis temperature. This shift occurs because the vibrational features associated with Al–O alkoxide linkages in the AEG film are converted to Al–O vibrations in Al_2O_3 domains in the Al_2O_3 /carbon composite film. This behavior is consistent with an increase in the ionic character of the Al–O bonding in Al_2O_3 .³⁹ The partially graphitized carbon domains are not observed in the infrared spectra because graphite shows little to no infrared absorbance.^{56,57}

A closer look at the infrared absorbance of the AEG alucone film between 1300 and 1700 cm^{-1} is shown in Figure 5. This

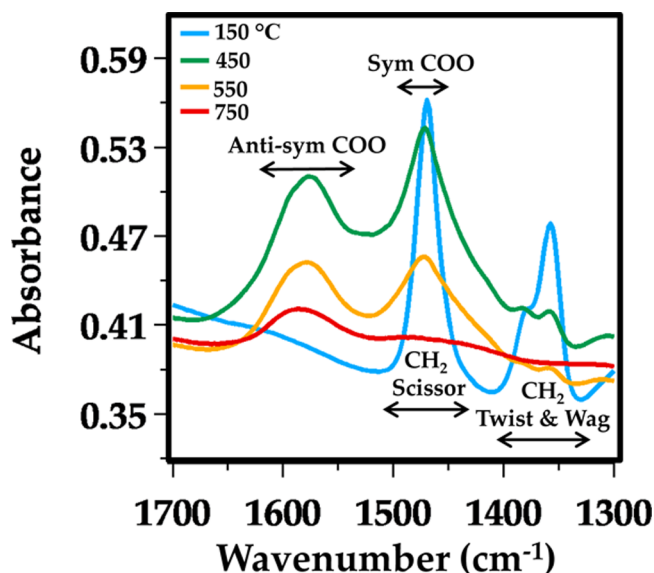


Figure 5. Expansion of FTIR spectra displayed in Figure 3 showing the effect of pyrolysis temperature on CH_2 scissors, CH_2 twist and wag, and carboxylate vibrational features between 1300 and 1700 cm^{-1} .

spectrum shows the only new infrared bands that appeared during the pyrolysis experiment. These absorbance features give insight into the species that exist at the interface between the Al_2O_3 and carbon domains. These features are attributed to the antisymmetric and symmetric stretching of carboxylate (R-COO^-) functionalities at 1570 and 1470 cm^{-1} , respectively.^{58–60}

The absorbance of the CH_2 scissoring mode and the symmetric COO stretch occur at essentially the same frequency of $\sim 1470 \text{ cm}^{-1}$. The existence of absorbance from the CH_2 scissors mode at higher temperatures can be ruled out by the disappearance of the other CH_2 vibrational modes. The absorbance of the CH_2 twist and wag modes between 1325 and 1400 cm^{-1} , also shown in Figure 5, decreases and disappears almost entirely by 550 $^\circ\text{C}$. However, the absorbance

at $\sim 1470 \text{ cm}^{-1}$ remains after pyrolysis at 600 $^\circ\text{C}$. This behavior indicates the presence of another species whose vibrational frequency occurs at approximately the same frequency.

Carboxylate species are common on Al_2O_3 surfaces.^{58,59} Metal carboxylate species have also been observed to form during the pyrolysis of alumina/polymer mixtures.⁶¹ Carboxylate groups can serve as an anchor for the carbonaceous residue formed from polymer thermal degradation.⁶¹ This stabilization on the metal oxide limits carbon species from more extensive decomposition and devolatilization.

A schematic picture of the Al_2O_3 /carbon composite is shown in Figure 6. This schematic displays Al_2O_3 domains and sp^2

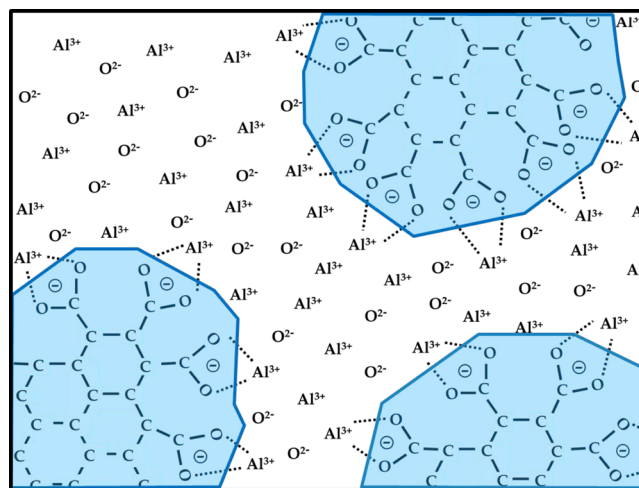


Figure 6. Schematic of interfacial Al_2O_3 /carbon composite film. The $\text{Al}^{3+}/\text{COO}^-$ interfacial species are at the border between the Al_2O_3 and carbon domains.

carbon domains. The aluminum carboxylate species are shown to exist at the interface between the Al_2O_3 and carbon domains. Partially graphitized carbon has been observed by Raman spectra recorded after the pyrolysis of alucone films formed using TMA and EG, glycerol, or HQ as the organic alcohol.¹⁵ This Al_2O_3 /carbon composite is also similar in structure to the nanodomained SiO_2 /carbon composite prepared by the pyrolysis of various organic siloxanes.⁶²

Figure 7 shows the normalized integrated absorbances of the C–H, C–C, C–O, and COO^- stretching vibrations versus temperature. Upon heating above 400 $^\circ\text{C}$, the infrared absorption of the C–H, C–C, and C–O bands decreases at approximately the same rate and disappears almost entirely by 500 $^\circ\text{C}$. In contrast, the infrared absorbance of the R-COO^- vibrational bands increases with temperatures up to 450 $^\circ\text{C}$. The absorbance of the carboxylate then slowly decreases up to 700 $^\circ\text{C}$.

The persistence of the carboxylate feature at high temperatures suggests that the aluminum carboxylate groups are intermediates in the reaction pathway. The reduction of the carboxylate features could indicate that the individual aluminum oxide and carbon domains begin to coalesce at higher temperatures. This coalescence would decrease the surface area available for the Al_2O_3 –carboxylate interaction.

EG is composed of two carbon atoms that will form the carbon domains during the pyrolysis of the AEG alucone films. These carbon domains could become conductive if they were connected to form a continuous pathway. However, Figure 3 shows that the background infrared absorbance of the AEG

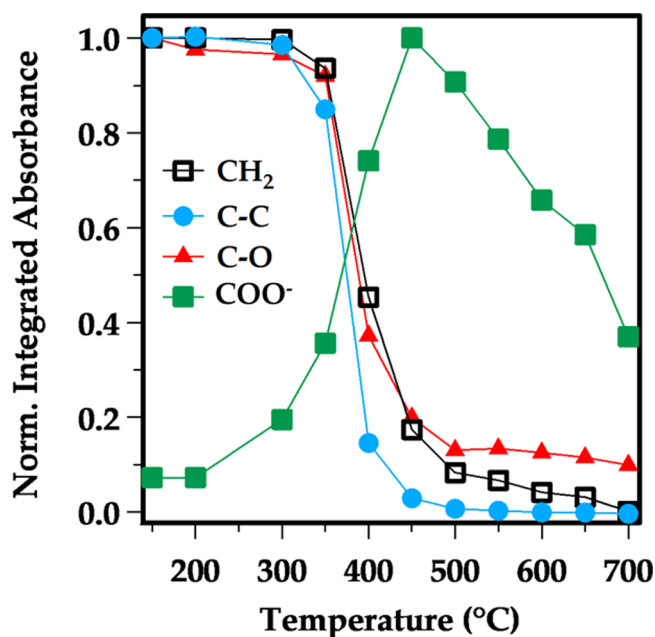


Figure 7. Normalized integrated absorbance of the CH_2 , C–C, C–O, and COO^- vibrational features in the AIEG alucone film versus pyrolysis temperature.

film did not increase during pyrolysis. The lack of increase in background absorbance suggests that these Al_2O_3 /carbon composites are not electrically conductive.

Recent sheet resistance measurements are also consistent with no electrical conductivity in pyrolyzed AIEG alucone films. The sheet resistances were too high to make accurate measurements.⁶³ In addition, XPS depth-profiling analysis of the pyrolyzed AIEG alucone films have observed low levels of carbon of <3 atom % after pyrolysis at 800 °C.⁶³ These sheet resistance and XPS depth-profiling measurements are consistent with low carbon concentrations in the pyrolyzed AIEG alucone films that are insufficient for electrical conductivity.

The carbon concentration of <3 atom % is much less than the expected carbon composition from the stoichiometry of the AIEG aluminum alkoxide polymer. Assuming an ideal AIEG polymer with a composition given by $\text{Al}_2(-\text{OCH}_2\text{CH}_2\text{O}-)_3$, the initial expected carbon concentration from XPS would be ~43 atom %. This estimated carbon concentration does not include H because H is not detected by XPS. The low carbon concentration of <3 atom % indicates that a significant amount of carbon present in the initial AIEG polymer is lost during pyrolysis.

B. Pyrolysis of AIHQ Alucone Films Grown Using TMA and HQ. Figure 8 shows the infrared absorbance of AIHQ alucone films prepared at 150 °C using 300 cycles of TMA and HQ versus pyrolysis temperature. The infrared absorbance of the C=C stretching vibrations of the phenylene ring at $\sim 1500\text{ cm}^{-1}$ is lost after pyrolysis at 450 °C. The C–H stretching vibrations at $3030\text{--}3065\text{ cm}^{-1}$ and the C–O stretching vibration at $1255\text{--}1290\text{ cm}^{-1}$ are also reduced after pyrolysis at 450 °C. The loss of these vibrational features is consistent with the decomposition of the original AIHQ film.

The most pronounced change in absorbance during pyrolysis at $>450\text{ °C}$ in Figure 8 is the increasing background infrared absorbance. The background infrared absorbance increases dramatically after pyrolysis at 550 and 650 °C. This increasing

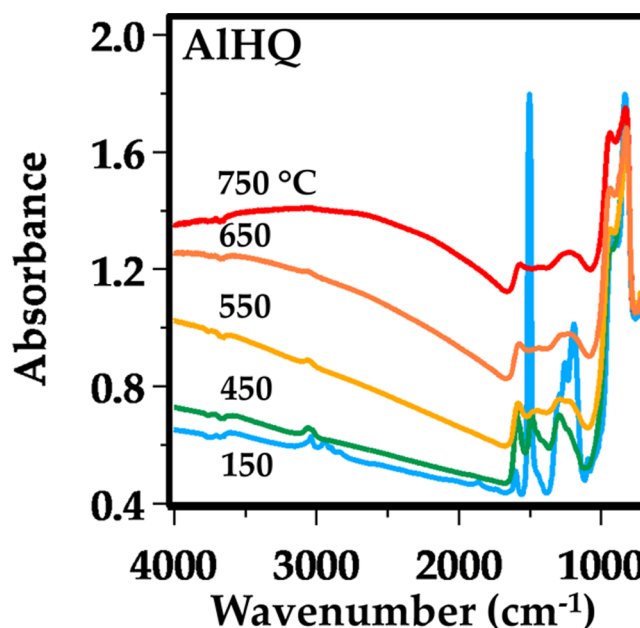


Figure 8. FTIR spectra of AIHQ alucone film grown using 300 cycles that was pyrolyzed at progressively higher temperatures up to 750 °C. These difference spectra are referenced to the initial ZrO_2 powder coated with 10 cycles of Al_2O_3 ALD.

background absorbance nearly overwhelms the other vibrational features after pyrolysis at 750 °C.

There is evidence of a carboxylate feature during the pyrolysis of the AIHQ alucone film. Figure 9 shows an expansion of Figure 8 in the wavelength region from 700 to 1900 cm^{-1} . The carboxylate feature is clearly visible after pyrolysis at 450 °C. The carboxylate peaks are present at 1475 and 1580 cm^{-1} .^{58–60} The analysis of this carboxylate feature at higher temperatures is complicated by the increase in the background absorbance.

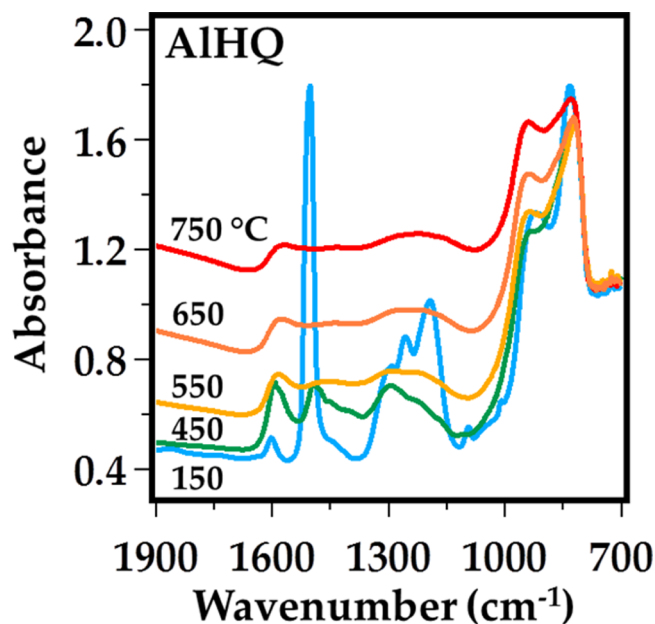


Figure 9. Expansion of FTIR spectra displayed in Figure 8 showing the effect of pyrolysis temperature on the vibrational features between 700 and 1900 cm^{-1} .

HQ is composed of six carbon atoms that will form the carbon domains after pyrolysis of the AlHQ alucone films. These carbon domains may form electrically conductive $\text{Al}_2\text{O}_3/\text{carbon}$ composites. The background infrared absorbance is directly related to electrical conductance. Free electron carriers contribute to the infrared absorption over the total infrared range. Any variation of the free electron carrier density translates into a change of the background infrared absorption.

Mathematically, the relationship between free electron carriers and infrared absorbance is described by the Drude–Zener theory.^{64,65} The Drude–Zener theory states that the absorbance at a given wavelength is related to the electrical conductivity according to^{64,65}

$$A(\lambda) = (\sigma(\lambda)z)/(\epsilon_0cn)$$

In this expression, $A(\lambda)$ is the absorbance at the wavelength, λ , and $\sigma(\lambda)$ is the electrical conductivity at the same wavelength. In addition, z is the thickness of the sample, ϵ_0 is the permittivity, c is the light velocity, and n is the refractive index of the material.

The increasing background infrared absorbance that occurs during AlHQ alucone film pyrolysis in Figures 8 and 9 can be attributed to an increase in the electrical conductivity of the film. Only small increases in the background absorbance are observed for pyrolysis temperatures up to 450 °C, where chemical restructuring is occurring. Above 500 °C, the absorbance increases progressively when electrically conducting carbon networks are forming. The background absorbance increase begins to level off at 750 °C after the formation of the conducting carbon domains.

These changes are consistent with recent studies on AlHQ alucone films that show decreasing electrical sheet resistance at pyrolysis temperatures above 500 °C.⁶³ Figure 10 shows the

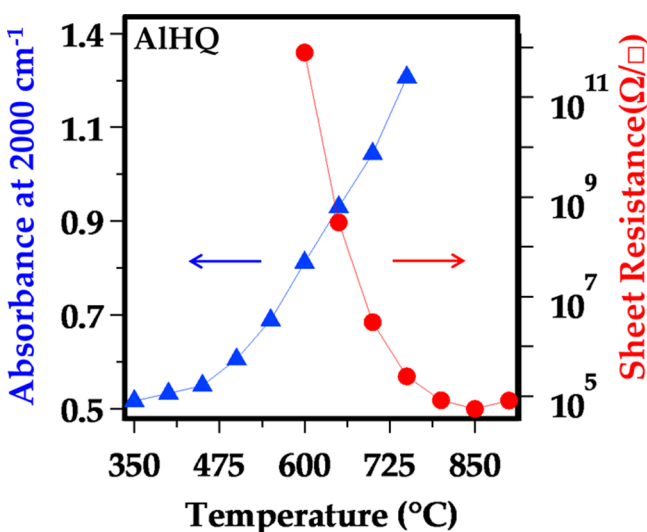


Figure 10. Comparison of background infrared absorbance measured at 2000 cm^{-1} and electrical sheet resistance of an AlHQ alucone film versus pyrolysis temperature.

correlation between the sheet resistance and background infrared absorbance data for AlHQ alucone films versus pyrolysis temperature. Because there are no absorption modes from vibrational species at 2000 cm^{-1} in the AlHQ alucone films, this frequency was used to measure the background infrared absorbance. The increase in background

infrared absorbance is correlated with a dramatic reduction of the sheet resistance of the film.

Figure 10 shows that the infrared absorbance increases from ~0.5 to ~1.3 from 350 to 730 °C. Over the same temperature range, the sheet resistance decreases from an immeasurably high sheet resistance to a sheet resistance of $\sim 2 \times 10^5 \text{ } \Omega/\square$.⁶³ This correlation illustrates the Drude–Zener relationship between electrical conductivity and infrared absorbance. After pyrolysis to higher temperatures of 850 °C, the AlHQ alucone films display an even lower sheet resistance of $5.6 \times 10^4 \text{ } \Omega/\square$ and a low electrical resistivity of 0.28 $\Omega \text{ cm}$.⁶³

These results demonstrate the importance of the choice of organic precursor used to grow the alucone films. To form an electrically conducting film, the organic precursor must contain enough carbon to form an electrically conducting network after pyrolysis. EG contains only two carbon atoms. The ALEG alucone films may lose too much carbon to provide a conducting carbon network after pyrolysis. Consequently, the pyrolyzed ALEG alucone films do not display an increase in their background infrared absorbance after pyrolysis.

In contrast, HQ contains six carbon atoms. The AlHQ alucone films have enough carbon to provide a conducting carbon network after pyrolysis. This conducting carbon network leads to an increase in the background infrared absorbance and decrease in the sheet resistance of the pyrolyzed AlHQ film. In agreement with this explanation, the XPS depth-profiling analysis of the pyrolyzed AlHQ alucone films measured high levels of carbon of ~48 atom % after pyrolysis at 800 °C.⁶³

The carbon concentration of ~48 atom % is somewhat less than the expected carbon composition from the stoichiometry of the AlHQ aluminum alkoxide polymer. Assuming an ideal AlHQ polymer with a composition given by $\text{Al}_2(-\text{OC}_6\text{H}_4\text{O}-)_3$, the initial expected carbon concentration from XPS would be ~69 atom % after neglecting the H component. The carbon concentration of ~48 atom % indicates that only a fraction of the carbon present in the initial AlHQ polymer is lost during pyrolysis.

The much higher carbon retention after pyrolysis for the AlHQ polymer compared with the ALEG polymer could be attributed to the initial state of carbon in the AlHQ polymer. Carbon is present in the AlHQ polymer in phenylene rings with sp^2 hybridization. This carbon is closer to the graphitic carbon in the $\text{Al}_2\text{O}_3/\text{carbon}$ composites that forms after pyrolysis than the carbon with sp^3 hybridization in the ALEG polymer. In addition, there is a higher carbon concentration in the AlHQ polymer that contains six carbons in each phenylene ring compared with the ALEG polymer that contains two carbons in each ethylene unit. If a fixed amount of carbon is consumed during pyrolysis, then a greater fraction of carbon would be lost from the ALEG polymers after pyrolysis.

Figure 11 displays the absorbance at 2000 cm^{-1} versus pyrolysis temperature for the ALEG and AlHQ alucone films. Both the ALEG and AlHQ films were grown using 300 cycles at 150 °C. The AlHQ alucone films show a dramatic increase in background absorbance at pyrolysis temperatures between 500 and 700 °C compared with the ALEG alucone films. The ALEG alucone films actually display a slight decrease in background infrared absorbance in Figure 11. This decrease is not the result of a conductivity decrease because the initial ALEG films are not electrically conductive. This decrease could be the result of sintering and a decrease in the amount of elastic light scattering occurring in the sample.

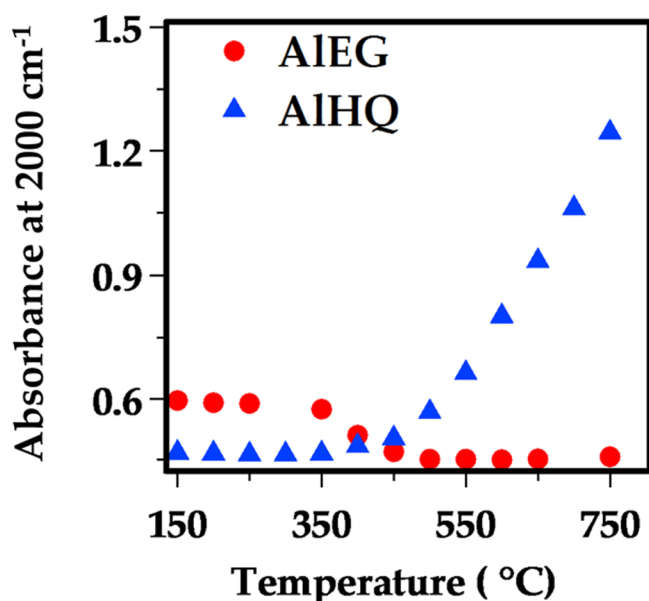


Figure 11. Background infrared absorbance measured at 2000 cm^{-1} for both AIEG and AIHQ alucone films versus pyrolysis temperature.

C. TEM Images of Pyrolyzed Alucone Films. One of the most important advantages of using ALD and MLD techniques is the excellent conformality of the deposited films on the initial substrate. Alucone MLD films display conformal deposition.¹⁹ The metal oxide/carbon composite films formed from the pyrolysis of MLD films may also maintain this conformality. If the conformality is retained after pyrolysis, then pyrolyzed MLD films could provide a pathway to deposit conformal conducting metal oxide/carbon composite films on high aspect ratio substrates.

To examine the conformality of the pyrolyzed alucone films, TEM images were recorded for pyrolyzed alucone films deposited on ZrO_2 particles. Figure 12a displays a TEM image of an AIEG alucone film pyrolyzed to $850\text{ }^\circ\text{C}$. Figure 12b displays a TEM image of an AIHQ alucone film pyrolyzed to $750\text{ }^\circ\text{C}$. These TEM images clearly show conformal films on the ZrO_2 particles. These images demonstrate that pyrolyzed alucone films maintain the conformality of the original alucone films.

This excellent conformality indicates that alucone films could be deposited on a variety of substrates and then pyrolyzed to yield conformal conducting Al_2O_3 /carbon composite films. These Al_2O_3 /carbon composites could have many applications for coating high surface area and high aspect ratio substrates. One possible application is for electrochemical substrates where the Al_2O_3 in the Al_2O_3 /carbon composite could provide electrode protection^{66,67} and the carbon in the Al_2O_3 /carbon composite could supply the required electrical conductivity.

IV. CONCLUSIONS

The growth and pyrolysis of alucone films grown using MLD techniques were studied using in situ transmission FTIR spectroscopy. The alucone films were grown using sequential exposures of TMA and either EG or HQ at $150\text{ }^\circ\text{C}$. The FTIR spectra of these AIEG and AIHQ alucone films were consistent with aluminum alkoxide polymer films. These alucone films were then pyrolyzed in vacuum at progressively higher temperatures. The FTIR spectra revealed pronounced differences between the AIEG and AIHQ alucone films.

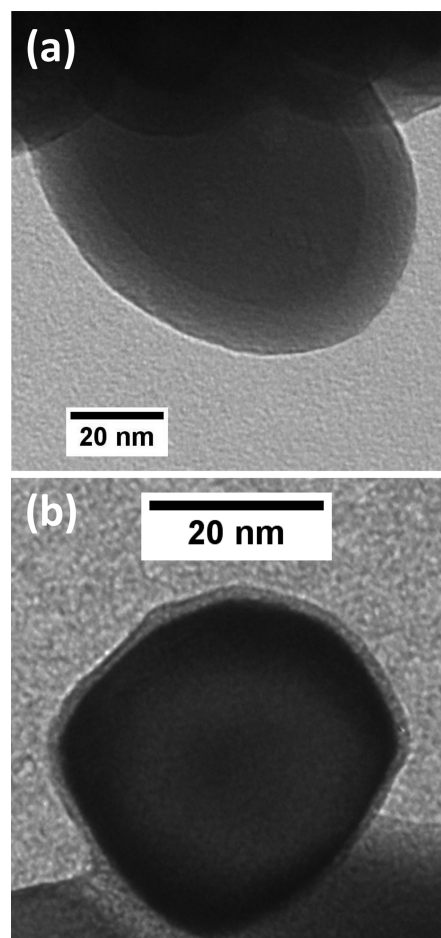


Figure 12. TEM images of (a) AIEG alucone film pyrolyzed to $850\text{ }^\circ\text{C}$ and (b) AIHQ alucone film pyrolyzed to $750\text{ }^\circ\text{C}$.

FTIR studies of the pyrolyzed AIEG alucone films showed that vibrational features related to C–H, C–C, and C–O stretching vibrations were lost by $500\text{ }^\circ\text{C}$. In addition, vibrational features corresponding to carboxylate species began to appear at $\sim 200\text{ }^\circ\text{C}$. The intensity of the carboxylate features progressively increased until $450\text{ }^\circ\text{C}$ and then decreased at temperatures up to $750\text{ }^\circ\text{C}$. The carboxylate species are believed to form at the interface between the Al_2O_3 and carbon domains in the Al_2O_3 /carbon composite film. These $\text{Al}^{3+}/\text{COO}^-$ species may help to stabilize the Al_2O_3 /carbon composite film. The background infrared absorbance of the AIEG films was not observed to increase during the pyrolysis experiments.

FTIR studies of the pyrolyzed AIHQ alucone films were very different from the pyrolyzed AIEG alucone films. The pyrolyzed AIHQ alucone films displayed a large increase in the background infrared absorbance with higher pyrolysis temperatures. This large increase in background infrared absorbance nearly overwhelmed the vibrational features of the pyrolyzed AIHQ film. The increase in the background infrared absorbance was attributed to the increased electrical conductivity of the AIHQ film resulting from the formation of conducting carbon domains during pyrolysis.

The correlation between electrical conductivity and background infrared absorbance is in accordance with Drude–Zener theory. The increase in background infrared absorbance correlated with the reduction of electrical sheet resistance for

the AlHQ alucone film. The differences between the pyrolysis of AIEG and AlHQ illustrate that the number of carbons in the initial organic precursors affects the amount of carbon in the pyrolyzed films and their resulting electrical conductivity. TEM images of the pyrolyzed AIEG and AlHQ alucone films showed extremely conformal films on the underlying ZrO_2 particles. These images illustrate that the conformality of the initial alucone MLD films is transferred to the pyrolyzed alucone films.

AUTHOR INFORMATION

Corresponding Author

*Phone: (303)-492-3398. E-mail: Steven.George@Colorado.edu.

Notes

The authors declare no competing financial interest.

ACKNOWLEDGMENTS

This research was funded by the National Science Foundation (CHE-1306131). We thank Jonathan J. Travis for measurements of electrical sheet resistance and for many helpful discussions.

REFERENCES

- (1) George, S. M. Atomic Layer Deposition: An Overview. *Chem. Rev.* **2010**, *110*, 111–131.
- (2) George, S. M.; Yoon, B.; Dameron, A. A. Surface Chemistry for Molecular Layer Deposition of Organic and Hybrid Organic-Inorganic Polymers. *Acc. Chem. Res.* **2009**, *42*, 498–508.
- (3) Puurunen, R. L. Surface Chemistry of Atomic Layer Deposition: A Case Study for the Trimethylaluminum/Water Process. *J. Appl. Phys.* **2005**, *97*, 121301.
- (4) Zhou, H.; Bent, S. F. Fabrication of Organic Interfacial Layers by Molecular Layer Deposition: Present Status and Future Opportunities. *J. Vac. Sci. Technol., A* **2013**, *31*, 040801.
- (5) George, S. M.; Lee, B. H.; Yoon, B.; Abdulagatov, A. I.; Hall, R. A. Metalcones: Hybrid Organic-Inorganic Films Fabricated Using Atomic and Molecular Layer Deposition Techniques. *J. Nanosci. Nanotechnol.* **2011**, *11*, 7948–7955.
- (6) Lee, B. H.; Yoon, B.; Abdulagatov, A. I.; Hall, R. A.; George, S. M. Growth and Properties of Hybrid Organic-Inorganic Metalcone Films Using Molecular Layer Deposition Techniques. *Adv. Funct. Mater.* **2013**, *23*, 532–546.
- (7) Jen, S. H.; George, S. M. Alucone Interlayers to Minimize Stress Caused by Thermal Expansion Mismatch between Al_2O_3 Films and Teflon Substrates. *ACS Appl. Mater. Interfaces* **2013**, *5*, 1165–1173.
- (8) Yoon, B.; Lee, B. H.; George, S. M. Highly Conductive and Transparent Hybrid Organic-Inorganic Zincone Thin Films Using Atomic and Molecular Layer Deposition. *J. Phys. Chem. C* **2012**, *116*, 24784–24791.
- (9) Lee, B. H.; Yoon, B.; Anderson, V. R.; George, S. M. Alucone Alloys with Tunable Properties Using Alucone Molecular Layer Deposition and Al_2O_3 Atomic Layer Deposition. *J. Phys. Chem. C* **2012**, *116*, 3250–3257.
- (10) Sundberg, P.; Karppinen, M. Organic and Inorganic-Organic Thin Film Structures by Molecular Layer Deposition: A Review. *Beilstein J. Nanotechnol.* **2014**, *5*, 1104–1136.
- (11) Liang, X. H.; Yu, M.; Li, J. H.; Jiang, Y. B.; Weimer, A. W. Ultrathin Microporous-Mesoporous Metal Oxide Films Prepared by Molecular Layer Deposition (MLD). *Chem. Commun.* **2009**, 7140–7142.
- (12) Ghazaryan, L.; Kley, E.-B.; Tuennermann, A.; Szeghalmi, A. V. Stability and Annealing of Alucones and Alucone Alloys. *J. Vac. Sci. Technol., A* **2013**, *31*, 01a149.
- (13) Liang, X.; Evanko, B. W.; Izar, A.; King, D. M.; Jiang, Y.-B.; Weimer, A. W. Ultrathin Highly Porous Alumina Films Prepared by Alucone ABC Molecular Layer Deposition (MLD). *Microporous Mesoporous Mater.* **2013**, *168*, 178–182.
- (14) Liang, X.; Li, J.; Yu, M.; McMurray, C. N.; Falconer, J. L.; Weimer, A. W. Stabilization of Supported Metal Nanoparticles Using an Ultrathin Porous Shell. *ACS Catal.* **2011**, *1*, 1162–1165.
- (15) Abdulagatov, A. I.; Terauds, K. E.; Travis, J. J.; Cavanagh, A. S.; Raj, R.; George, S. M. Pyrolysis of Titanicone Molecular Layer Deposition Films as Precursors for Conducting TiO_2 /Carbon Composite Films. *J. Phys. Chem. C* **2013**, *117*, 17442–17450.
- (16) Colombo, P.; Mera, G.; Riedel, R.; Sorarù, G. D. Polymer-Derived Ceramics: 40 Years of Research and Innovation in Advanced Ceramics. *J. Am. Ceram. Soc.* **2010**, *1837*, 1805–1837.
- (17) Yang, P.; Wang, G.; Gao, Z.; Chen, H.; Wang, Y.; Qin, Y. Uniform and Conformal Carbon Nanofilms Produced Based on Molecular Layer Deposition. *Materials* **2013**, *6*, 5602–5612.
- (18) Riedel, R.; Mera, G.; Hauser, R.; Kloneczynski, A. Silicon-Based Polymer-Derived Ceramics: Synthesis Properties and Applications-A Review. *J. Ceram. Soc. Jpn.* **2006**, *114*, 425–444.
- (19) Dameron, A. A.; Seghete, D.; Burton, B. B.; Davidson, S. D.; Cavanagh, A. S.; Bertrand, J. A.; George, S. M. Molecular Layer Deposition of Alucone Polymer Films Using Trimethylaluminum and Ethylene Glycol. *Chem. Mater.* **2008**, *20*, 3315–3326.
- (20) Peng, Q.; Gong, B.; VanGundy, R. M.; Parsons, G. N. "Zincone" Zinc Oxide-Organic Hybrid Polymer Thin Films Formed by Molecular Layer Deposition. *Chem. Mater.* **2009**, *21*, 820–830.
- (21) Yoon, B.; O'Patchen, J. L.; Seghete, D.; Cavanagh, A. S.; George, S. M. Molecular Layer Deposition of Hybrid Organic-Inorganic Polymer Films using Diethylzinc and Ethylene Glycol. *Chem. Vap. Depos.* **2009**, *15*, 112–121.
- (22) Lee, B. H.; Anderson, V. R.; George, S. M. Molecular Layer Deposition of Zirconium and ZrO_2 /Zirconium Alloy Films: Growth and Properties. *Chem. Vap. Depos.* **2013**, *19*, 204–212.
- (23) Lee, B. H.; Anderson, V. R.; George, S. M. Growth and Properties of Hafnicones and HfO_2 /Hafnicones Nanolaminate and Alloy Films Using Molecular Layer Deposition Techniques. *ACS Appl. Mater. Interfaces* **2014**, *6*, 16880–16887.
- (24) Abdulagatov, A. I.; Hall, R. A.; Sutherland, J. L.; Lee, B. H.; Cavanagh, A. S.; George, S. M. Molecular Layer Deposition of Titanicone Films using TiCl_4 and Ethylene Glycol or Glycerol: Growth and Properties. *Chem. Mater.* **2012**, *24*, 2854–2863.
- (25) Brown, J. J.; Hall, R. A.; Kladiotis, P. E.; George, S. M.; Bright, V. M. Molecular Layer Deposition on Carbon Nanotubes. *ACS Nano* **2013**, *7*, 7812–7823.
- (26) Jen, S. H.; Lee, B. H.; George, S. M.; McLean, R. S.; Garcia, P. F. Critical Tensile Strain and Water Vapor Transmission Rate for Nanolaminate Films Grown Using Al_2O_3 Atomic Layer Deposition and Alucone Molecular Layer Deposition. *Appl. Phys. Lett.* **2012**, *101*, 234103.
- (27) Sun, F. B.; Duan, Y.; Yang, Y. Q.; Chen, P.; Duan, Y. H.; Wang, X.; Yang, D.; Xue, K. W. Fabrication of Tunable Al_2O_3 : Alucone Thin-Film Encapsulations for Top-Emitting Organic Light-Emitting Diodes with High Performance Optical and Barrier Properties. *Org. Electron.* **2014**, *15*, 2546–2552.
- (28) Vaha-Nissi, M.; Sundberg, P.; Kauppi, E.; Hirvikorpi, T.; Sievanen, J.; Sood, A.; Karppinen, M.; Harlin, A. Barrier Properties of Al_2O_3 and Alucone Coatings and Nanolaminates on Flexible Biopolymer Films. *Thin Solid Films* **2012**, *520*, 6780–6785.
- (29) Yu, M. A.; Funke, H. H.; Noble, R. D.; Falconer, J. L. H_2 Separation Using Defect-Free, Inorganic Composite Membranes. *J. Am. Chem. Soc.* **2011**, *133*, 1748–1750.
- (30) Seghete, D.; Davidson, B. D.; Hall, R. A.; Chang, Y. J.; Bright, V. M.; George, S. M. Sacrificial Layers for Air Gaps in NEMS Using Alucone Molecular Layer Deposition. *Sens. Actuators, A* **2009**, *155*, 8–15.
- (31) Piper, D. M.; Travis, J. J.; Young, M.; Son, S.-B.; Kim, S. C.; Oh, K. H.; George, S. M.; Ban, C.; Lee, S.-H. Reversible High-Capacity Si Nanocomposite Anodes for Lithium-Ion Batteries Enabled by Molecular Layer Deposition. *Adv. Mater.* **2014**, *26*, 1596–1601.

- (32) Li, X.; Lushington, A.; Liu, J.; Li, R.; Sun, X. Superior Stable Sulfur Cathodes of Li-S Batteries Enabled by Molecular Layer Deposition. *Chem. Commun.* **2014**, *50*, 9757–9760.
- (33) Adamczyk, N. M.; Dameron, A. A.; George, S. M. Molecular Layer Deposition of Poly(P-Phenylene Terephthalamide) Films Using Terephthaloyl Chloride and P-Phenylenediamine. *Langmuir* **2008**, *24*, 2081–2089.
- (34) Ferguson, J. D.; Weimer, A. W.; George, S. M. Atomic Layer Deposition of Ultrathin and Conformal Al₂O₃ films on BN Particles. *Thin Solid Films* **2000**, *371*, 95–104.
- (35) Ballinger, T. H.; Wong, J. C. S.; Yates, J. T. Transmission Infrared-Spectroscopy of High Area Solid-Surfaces - A Useful Method for Sample Preparation. *Langmuir* **1992**, *8*, 1676–1678.
- (36) Lewis, B. F.; Bowser, W. M.; H, J. L., Jr.; Luu, T.; Weinberg, W. H. Inelastic Electron Tunneling Spectroscopy of Phenol and Hydroquinone Chemisorbed on Alumina. *J. Vac. Sci. Technol.* **1974**, *11*, 262–265.
- (37) Tzeng, W. B.; Narayanan, K.; Hsieh, C. Y.; Tung, C. C. A Study of the Excited State Structure and Vibrations of Hydroquinone by Ab Initio Calculations and Resonant Two-Photon Ionization Spectroscopy. *Spectrochim. Acta, Part A* **1997**, *53*, 2595–2604.
- (38) Brüesch, P.; Kötzt, R.; Neff, H.; Pietronero, L. Vibrational Properties of Al₂O₃ Films on Gold, Aluminum, and Silicon. *Phys. Rev. B* **1984**, *29*, 4691–4696.
- (39) Johnson, R. S.; Lucovsky, G.; Baumvol, I. Physical and Electrical Properties of Noncrystalline Al₂O₃ Prepared by Remote Plasma Enhanced Chemical Vapor Deposition. *J. Vac. Sci. Technol., A* **2001**, *19*, 1353–1353.
- (40) Wilson, E. B. The Normal Modes and Frequencies of Vibration of the Regular Plane Hexagon Model of the Benzene Molecule. *Phys. Rev.* **1934**, *45*, 0706–0714.
- (41) Lewis, I. C. Chemistry of Carbonization. *Carbon* **1982**, *20*, 519–529.
- (42) Gilbert, J. B.; Kipling, J. J.; McEnaney, B.; Sherwood, J. N. Carbonization of Polymers I– Thermogravimetric Analysis. *Polymer* **1962**, *3*, 1–10.
- (43) Lewis, I. C. Chemistry of Pitch Carbonization. *Fuel* **1987**, *66*, 1527–1531.
- (44) Winslow, F. H.; Baker, W. O.; Yager, W. A. The Structure and Properties of Some Pyrolyzed Polymers. *Proc. Conf. Carbon* **1955**, 93–102.
- (45) Fu, P.; Hu, S.; Xiang, J.; Li, P.; Huang, D.; Jiang, L.; Zhang, A.; Zhang, J. FTIR Study of Pyrolysis Products Evolving from Typical Agricultural Residues. *J. Anal. Appl. Pyrolysis* **2010**, *88*, 117–123.
- (46) Fu, P.; Hu, S.; Xiang, J.; Sun, L.; Yang, T.; Zhang, A.; Zhang, J. Mechanism Study of Rice Straw Pyrolysis by Fourier Transform Infrared Technique. *Chin. J. Chem. Eng.* **2009**, *17*, 522–529.
- (47) Otani, S. On the Carbon Fiber from the Molten Pyrolysis Products. *Carbon* **1965**, *3*, 31–38.
- (48) Ko, T. H.; Kuo, W. S.; Chang, Y. H. Raman Study of the Microstructure Changes of Phenolic Resin During Pyrolysis. *Polym. Compos.* **2000**, *21*, 745–750.
- (49) Trchova, M.; Matejka, P.; Brodinova, J.; Kalendova, A.; Prokes, J.; Stejskal, J. Structural and Conductivity Changes During the Pyrolysis of Polyaniline Base. *Polym. Degrad. Stab.* **2006**, *91*, 114–121.
- (50) Hudson, M. J.; Peckett, J. W.; Sibley, C. S.; Harris, P. J. F. Pyrolysis of Polymer-Derived Carbons in the Formation of Graphitizing Carbons and Nanoparticles of Zirconia. *Ind. Eng. Chem. Res.* **2008**, *47*, 2605–2611.
- (51) Naka, K.; Nagae, H.; Ichiyanagi, M.; Jeong, O. C.; Konishi, S. Investigation of Pyrolyzed Polyimide Thin Film as MEMS Material. *J. Semicond. Technol. Sci.* **2005**, *5*, 38–44.
- (52) Schueller, O. J. A.; Brittain, S. T.; Whitesides, G. M. Fabrication of Glassy Carbon Microstructures by Pyrolysis of Microfabricated Polymeric Precursors. *Adv. Mater.* **1997**, *9*, 477–480.
- (53) Wang, Y.; Santiago-Aviles, J. J.; Furlan, R.; Ramos, I. Pyrolysis Temperature and Time Dependence of Electrical Conductivity Evolution for Electrostatically Generated Carbon Nanofibers. *IEEE Trans. Nanotechnol.* **2003**, *2*, 39–43.
- (54) Blaszkiewicz, M.; McLachlan, D. S.; Newnham, R. E. The Volume Fraction and Temperature Dependence of the Resistivity in Carbon Black and Graphite Polymer Composites: An effective Media-Percolation Approach. *Polym. Eng. Sci.* **1992**, *32*, 421–425.
- (55) McLachlan, D. S.; Blaszkiewicz, M.; Newnham, R. E. Electrical Resistivity of Composites. *J. Am. Ceram. Soc.* **1990**, *73*, 2187–2203.
- (56) Gomez-Serrano, V.; Pastor-Villegas, J.; Perez-Florindo, A.; Duran-Valle, C.; Valenzuela-Calahorra, C. FT-IR Study of Rockrose and of Char and Activated Carbon. *J. Anal. Appl. Pyrolysis* **1996**, *36*, 71–80.
- (57) Friedel, R. A.; C, G. L. Infrared Spectra of Ground Graphite. *J. Phys. Chem.* **1971**, *76*, 15–17.
- (58) Dobson, K. D.; McQuillan, A. J. In Situ Infrared Spectroscopic Analysis of the Adsorption of Aliphatic Carboxylic Acids to TiO₂, ZrO₂, Al₂O₃, and Ta₂O₅ from Aqueous Solutions. *Spectrochim. Acta, Part A* **1999**, *55*, 1395–1405.
- (59) Tong, S. R.; Wu, L. Y.; Ge, M. F.; Wang, W. G.; Pu, Z. F. Heterogeneous Chemistry of Monocarboxylic Acids on Alpha-Al₂O₃ at Different Relative Humidities. *Atmos. Chem. Phys.* **2010**, *10*, 7561–7574.
- (60) Yoon, B.; Seghete, D.; Cavanagh, A. S.; George, S. M. Molecular Layer Deposition of Hybrid Organic-Inorganic Alucone Polymer Films Using a Three-Step ABC Reaction Sequence. *Chem. Mater.* **2009**, *21*, 5365–5374.
- (61) Higgins, R. J.; Rhine, W. E.; Cima, M. J.; Bowen, H. K.; Farneth, W. E. Ceramic Surface Reactions and Carbon Retention during Non-Oxidative Binder Removal Al₂O₃/Poly(methyl methacrylate) at 20–700C. *J. Am. Ceram. Soc.* **1994**, *77*, 2243–2254.
- (62) Saha, A.; Raj, R.; Williamson, D. L. A Model for the Nanodomains in Polymer-Derived SiCO. *J. Am. Ceram. Soc.* **2006**, *89*, 2188–2195.
- (63) Travis, J. J.; George, S. M., unpublished results.
- (64) Kahn, A. Theory of the Infrared Absorption of Carriers in Germanium and Silicon. *Phys. Rev.* **1955**, *97*, 1647–1652.
- (65) Baraton, M.-I.; Merhari, L. Determination of the Gas Sensing Potentiality of Nanosized Powders by FTIR Spectrometry. *Scr. Mater.* **2001**, *44*, 1643–1648.
- (66) Jung, Y. S.; Cavanagh, A. S.; Dillon, A. C.; Groner, M. D.; George, S. M.; Lee, S.-H. Enhanced Stability of LiCoO₂ Cathodes in Lithium-Ion Batteries Using Surface Modification by Atomic Layer Deposition. *J. Electrochem. Soc.* **2010**, *157*, A75–A81.
- (67) Scott, I. D.; Jung, Y. S.; Cavanagh, A. S.; An, Y.; Dillon, A. C.; George, S. M.; Lee, S.-H. Ultrathin Coatings on Nano-LiCoO₂ for Li-Ion Vehicular Applications. *Nano Lett.* **2011**, *11*, 414–418.